JACS
JOURNAL OF THE AMERICAN CHEMICAL SOCIETY

Communication

pubs.acs.org/JACS

Tailor-Made Pore Surface Engineering in Covalent Organic Frameworks: Systematic Functionalization for Performance Screening

Ning Huang,[†] Rajamani Krishna,[‡] and Donglin Jiang*[,†]

[†]Department of Materials Molecular Science, Institute for Molecular Science, National Institutes of Natural Sciences, 5-1 Higashiyama, Myodaiji, Okazaki 444-8787, Japan

[‡]Van't Hoff Institute for Molecular Sciences, University of Amsterdam, Science Park 904, 1098 XH Amsterdam, The Netherlands

Supporting Information

ABSTRACT: Imine-linked covalent organic frameworks (COFs) were synthesized to bear content-tunable, accessible, and reactive ethynyl groups on the walls of one-dimensional pores. These COFs offer an ideal platform for pore-wall surface engineering aimed at anchoring diverse functional groups ranging from hydrophobic to hydrophilic units and from basic to acidic moieties with controllable loading contents. This approach enables the development of various tailor-made COFs with systematically tuned porosities and functionalities while retaining the crystallinity. We demonstrate that this strategy can be used to efficiently screen for suitable pore structures for use as CO_2 adsorbents. The pore-surface-engineered walls exhibit an enhanced affinity for CO_2, resulting in COFs that can capture and separate CO_2 with high performance.

Covalent organic frameworks (COFs) are an emerging class of crystalline porous polymers with pre-designable porous structure.[1] The ordered open channels found in two-dimensional (2D) COFs could render them able to adsorb CO_2. However, the COFs' dense layer architecture results in low porosity that has thus far restricted their potential for CO_2 adsorption.[2−7] Here, we describe the use of pore surface engineering to overcome these limitations by anchoring functional groups to the pore walls to enhance the affinity of the COFs for CO_2. This method integrates a variety of functionalities with controllable loading contents onto the pore walls, which efficiently screen for structures that are suitable for CO_2 capture.

Among various types of COFs, imine-linked COFs are stable under various conditions, making them attractive for CO_2 adsorption.[2d,f,5,6e] However, conventional imine-linked COFs usually exhibit low CO_2 capacities. The conversion of imine-linked COFs into high-performance CO_2-adsorption materials is highly desired but has yet to be fully explored.

We utilized a mesoporous imine-linked porphyrin COF with a low capacity for CO_2 adsorption as a scaffold (Scheme 1). We developed a three-component reaction system consisting of 5,10,15,20-tetrakis(*p*-tetraphenylamino)porphyrin and a mixture of 2,5-bis(2-propynyloxy)terephthalaldehyde (BPTA) and 2,5-dihydroxyterephthalaldehyde (DHTA) at various molar ratios (X = [BPTA]/([BPTA] + [DHTA]) × 100 = 0, 25, 50, 75, and 100) for the synthesis of four COFs with different ethynyl contents on their edges (Scheme 1, $[HC{\equiv}C]_X$-H_2P-COFs, X = 25, 50, 75, and 100). Quantitative click reactions between the ethynyl units and azide compounds were performed to anchor the desired groups onto the pore walls (Scheme 1, Supporting Information). We synthesized 20 different COFs with pores functionalized with a variety of functional groups, including ethyl, acetate, hydroxyl, carboxylic acid, and amino groups; these groups ranged from hydrophobic to hydrophilic and from basic to acidic (Scheme 1, $[R]_X$-H_2P-COFs ($[Et]_X$-H_2P-COFs, $[MeOAc]_X$-H_2P-COFs, $[EtOH]_X$-H_2P-COFs, $[AcOH]_X$-H_2P-COFs, $[EtNH_2]_X$-H_2P-COFs)).

Infrared (IR) spectroscopy provides direct evidence for the presence of ethynyl units in $[HC{\equiv}C]_X$-H_2P-COFs and functionalized groups in $[R]_X$-H_2P-COFs (Figure S1).[3a] Elemental analysis revealed that the actual ethynyl and functional unit contents of the COFs were close to the calculated values (Table S1). X-ray diffraction (XRD) measurements (Figure S2) revealed that $[HC{\equiv}C]_X$-H_2P-COFs and H_2P-COF exhibited the same XRD pattern, thereby demonstrating that the crystal structure of H_2P-COF was retained. The pore-surface-engineered COFs also exhibited the same XRD patterns as H_2P-COF (Figure S2), indicating that the crystalline framework was retained. Scheme 1B presents the pore structures of $[HC{\equiv}C]_{100}$-H_2P-COF, $[Et]_{100}$-H_2P-COF, $[MeOAc]_{100}$-H_2P-COF, $[EtOH]_{100}$-H_2P-COF, $[AcOH]_{100}$-H_2P-COF, and $[EtNH_2]_{100}$-H_2P-COF. The porous structures of these COFs can be fully changed through the integration of different functional groups.

Nitrogen sorption isotherms were collected at 77 K to investigate the porosity of the COFs (Figure S3). The $[HC{\equiv}C]_X$-H_2P-COFs exhibited Brunauer−Emmett−Teller (BET) surface areas of 1474, 1413, 962, 683, and 462 $m^2\ g^{-1}$, corresponding to ethynyl content (X) of 0, 25, 50, 75, and 100, respectively (Table S2). This trend indicates that the ethynyl groups occupied the pore space. As a result, the pore volume decreased from 0.75 to 0.71, 0.57, 0.42, and 0.28 $cm^3\ g^{-1}$, respectively. Notably, these COFs contained only one type of pore in the framework (Figure S4), indicating that the ethynyl units were randomly integrated into the pore walls of $[HC{\equiv}$

Received: April 25, 2015
Published: May 30, 2015

DOI: 10.1021/jacs.5b04300
J. Am. Chem. Soc. 2015, 137, 7079−7082

Scheme 1. (A) Schematic of Pore Surface Engineering of Imine-Linked COFs with Various Functional Groups via Click Reactions; (B) Pore Structures of COFs with Different Functional Groups (Gray, C; Blue, N; Red, O)

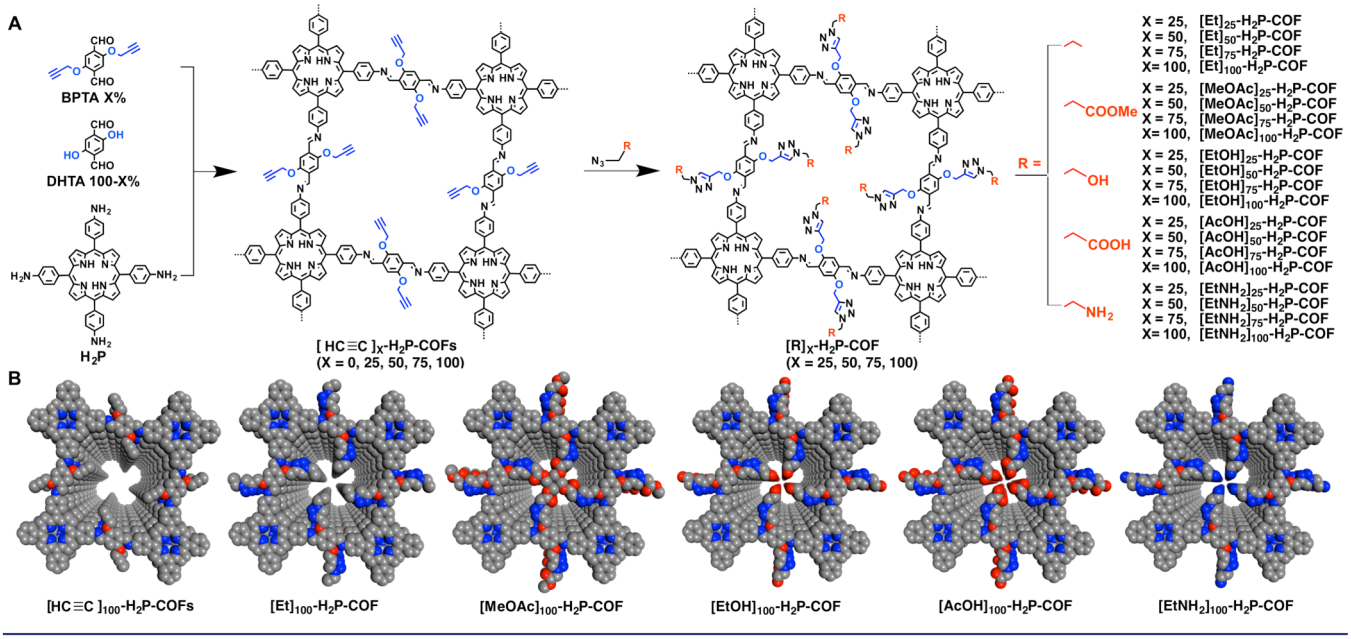

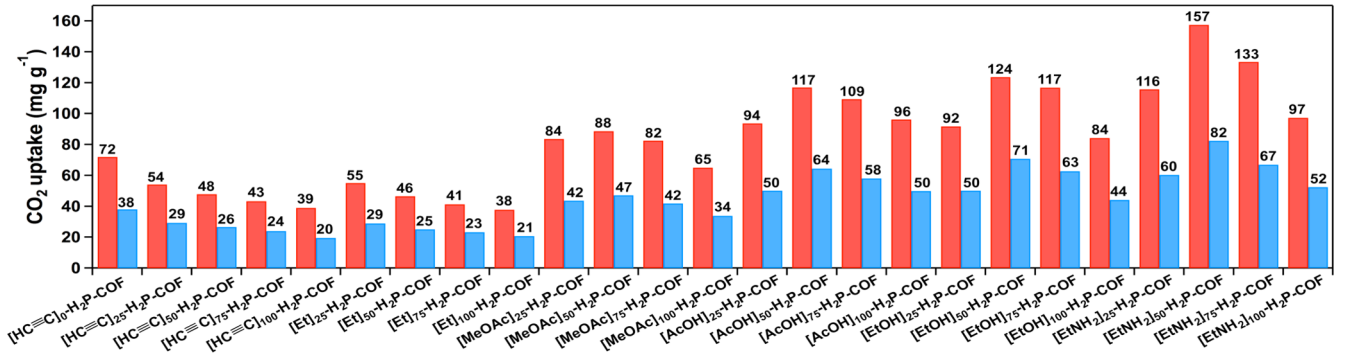

Figure 1. Carbon dioxide adsorption capacity of the COFs at 273 (red) and 298 K (blue) and 1 bar.

$C]_X$-H_2P-COFs (X = 25, 50, and 75). The pore size decreased from 2.5 to 2.3, 2.1, 1.9, and 1.6 nm as the X value was increased from 0 to 25, 50, 75, and 100, respectively (Table S2).

Compared to $[HC{\equiv}C]_X$-H_2P-COFs, the $[Et]_X$-H_2P-COFs with the same X value exhibited more explicit decrease in their BET surface areas, pore volumes, and pore sizes (Figure S3, Table S2). These decrease resulted from the occupation of the pores by longer chains that were integrated via pore surface engineering (Scheme 1B). For example, for $[Et]_{25}$-H_2P-COF, $[Et]_{50}$-H_2P-COF, $[Et]_{75}$-H_2P-COF, and $[Et]_{100}$-H_2P-COF, the BET surface areas were 1326, 821, 485, and 187 $m^2\ g^{-1}$, and the pore volumes were 0.55, 0.48, 0.34, and 0.18 $cm^3\ g^{-1}$, respectively. The pore surface engineering steadily decreased the pore size from a mesopore to supermicropores, allowing the systematic tuning of the pore sizes from 2.2 to 1.9, 1.6, and 1.5 nm. Such fine adjustments of the pore size have not been achieved via direct polycondensation. Upon pore-wall engineering with ester, hydroxyl, carboxylic acid, and amino groups, the BET surface areas, pore volumes, and pore sizes of the resulting $[MeOAc]_X$-H_2P-COFs, $[EtOH]_X$-H_2P-COFs, $[AcOH]_X$-H_2P-COFs, and $[EtNH_2]_X$-H_2P-COFs exhibited similar tendencies to decrease compared to those of the $[Et]_X$-H_2P-COFs.

The systematic integration of functional groups, in combination with a significant decrease in the pore size, makes the resulting COFs attractive for CO_2 adsorption (Figures S5 and S6). $[HC{\equiv}C]_X$-H_2P-COFs with the X values of 0, 25, 50, 75, and 100 exhibited CO_2 capacity of 38, 29, 26, 24, and 20 mg g^{-1}, respectively, at 298 K and 1 bar; these capacities increased to 72, 54, 48, 43, and 39 mg g^{-1} at 273 K and 1 bar (Figure 1). These results indicate that the $[HC{\equiv}C]_X$-H_2P-COFs are conventional COFs with low adsorption capacities. We observed that the capacity for CO_2 adsorption was highly dependent on the structures of the functional groups. Upon the introduction of ethyl units onto the pore walls, the resulting $[Et]_X$-H_2P-COFs (X = 25, 50, 75, and 100) exhibited CO_2 adsorption capacities similar to those of the $[HC{\equiv}C]_X$-H_2P-COFs under otherwise identical conditions (Figure 1). By contrast, when the functional groups were changed to ester units, the $[MeOAc]_X$-H_2P-COFs exhibited enhanced CO_2 adsorption capacities. $[MeOAc]_{50}$-H_2P-COF exhibites the highest capacity among the $[MeOAc]_X$-H_2P-COFs, with CO_2 adsorption capacities of 47 and 88 mg g^{-1} at 298 and 273 K, respectively (Figure 1).These values are 1.6-fold greater than those of the best-performing $[Et]_X$-H_2P-COFs. Notably, the introduction of carboxylic acid groups

DOI: 10.1021/jacs.5b04300
J. Am. Chem. Soc. 2015, 137, 7079−7082

greatly enhanced the capacity. The capacities of $[AcOH]_{25}$-H_2P-COF, $[AcOH]_{50}$-H_2P-COF, $[AcOH]_{75}$-H_2P-COF, and $[AcOH]_{100}$-H_2P-COF were 50, 64, 58, and 50 mg g^{-1} at 298 K and 94, 117, 109, and 96 mg g^{-1} at 273 K, respectively (Figure 1). The integration of hydroxyl groups similarly enhanced the adsorption. For example, $[EtOH]_{50}$-H_2P-COF exhibited capacities of 71 and 124 mg g^{-1} at 298 and 273 K, respectively, which are 2.3- to 2.4-fold greater than the capacities of $[HC{\equiv}C]_{25}$-H_2P-COF. Surprisingly, pore surface engineering with the amino groups led to an overall enhancement of CO_2 adsorption (Figure 1). The capacities of $[EtNH_2]_{25}$-H_2P-COF, $[EtNH_2]_{50}$-H_2P-COF, $[EtNH_2]_{75}$-H_2P-COF, and $[EtNH_2]_{100}$-H_2P-COF were 60, 82, 67, and 52 mg g^{-1} at 298 K and 116, 157, 133, and 97 mg g^{-1} at 273 K, respectively. $[EtNH_2]_{50}$-H_2P-COF exhibited the highest adsorption capacity, which was almost 3-fold greater than those of $[Et]_{50}$-H_2P-COF and $[HC{\equiv}C]_{50}$-H_2P-COF.

The dramatic change in the adsorption of CO_2 upon pore surface engineering is related to the interactions between functional groups and CO_2. The nonpolar ethynyl and ethyl groups interact weakly with CO_2, resulting in their poor adsorption capacity. By contrast, the polar ester units could interact with CO_2 via dipole interactions and thus improve the affinity of the COF for CO_2. The enhanced capacities of $[AcOH]_X$-H_2P-COFs and $[EtOH]_X$-H_2P-COFs resulted from the dipole and hydrogen bonding interactions of carboxylic and hydroxyl units with CO_2. The amino groups can form acid–base pairs with CO_2, leading to a significant enhancement in CO_2 adsorption. COFs with the same functional groups show two different tendencies with respect to CO_2 adsorption. The first class is the $[Et]_X$-H_2P-COFs, in which the pore walls have fewer interactions with CO_2 and thus exhibit a simple decrease in CO_2 adsorption capacity with X values because of their decreased surface areas and pore volumes. The second class consists of the $[MeOAc]_X$-H_2P-COFs, $[AcOH]_X$-H_2P-COFs, $[EtOH]_X$-H_2P-COFs, and $[EtNH_2]_X$-H_2P-COFs, which all interact strongly with CO_2 and exhibit maximal capacities at $X = 50$. This behavior is the result of a balance between the two contradictory effects of enhanced affinity and decreased porosity on adsorption. This type of perturbation indicates that precise pore surface engineering is a key component of capturing CO_2 with COFs.

To elucidate the nature of the CO_2 adsorption, we calculated the isosteric heat of adsorption (Q_{st}) from the CO_2 adsorption isotherm curves collected at pressures as high as 1 bar and at temperatures of 273 and 298 K (Table S2). Interestingly, the Q_{st} value increased in the order of $[HC{\equiv}C]_X$-H_2P-COFs ≈ $[Et]_X$-H_2P-COFs < $[MeOAc]_X$-H_2P-COFs < $[AcOH]_X$-H_2P-COFs < $[EtOH]_X$-H_2P-COFs < $[EtNH_2]_X$-H_2P-COFs (Table S2). For example, $[HC{\equiv}C]_X$-H_2P-COFs and $[Et]_X$-H_2P-COFs had Q_{st} values of 15.3–16.8 kJ mol^{-1}. The Q_{st} values of $[MeOAc]_X$-H_2P-COFs were higher, ranging between 16.4 and 17.8 kJ mol^{-1}. More significant enhancements in the Q_{st} values were observed for $[AcOH]_X$-H_2P-COFs and $[EtOH]_X$-H_2P-COFs; these COFs had Q_{st} values of 17.7–18.8 and 18.2–19.3 kJ mol^{-1}, respectively. $[EtNH_2]_X$-H_2P-COFs exhibited the highest Q_{st} values, which ranged from 20.4 to 20.9 kJ mol^{-1}. These results indicate that the COFs with the strongest affinity for CO_2 were those with pore walls that were functionalized with amino groups; those groups facilitated the adsorption of CO_2 and contributed to the enhanced CO_2 adsorption performance (ideal adsorbed solution theory (IAST) calculations of selectivity, see Figure S7).

To evaluate the gas adsorption capability of adsorbents under kinetic flowing gas conditions (CO_2/N_2 mixture containing 15% CO_2 and 85% N_2, 298 K, 100 kPa), we performed breakthrough simulations using a precise methodology established by Krishna and Long (Supporting Information, Tables S4 and S5, Figures S8 and S9).[8] These simulations accurately reflect the separation ability of a pressure-swing adsorption (PSA) process, which is an energetically efficient method for industrial-scale capture. Figure 2A shows a schematic of a packed-bed absorber. Figure 2B,C presents typical breakthrough curves for $[HC{\equiv}C]_{50}$-H_2P-COF and $[EtNH_2]_{50}$-H_2P-COF, respectively, where the x-axis is dimensionless time, τ, which is defined as the division of actual time t by the characteristic time $L\varepsilon/\mu$ (Supporting Information). $[EtNH_2]_{50}$-H_2P-COF exhibited a breakthrough time of 25, which was much longer than that of $[HC{\equiv}C]_{50}$-H_2P-COF (7). Figure 2D compares the breakthrough characteristics of the two COFs in terms of CO_2 concentration (mol%) at the absorber outlet, which is depicted as a function of dimensionless time when the operation was performed at a total pressure of 100 kPa. $[EtNH_2]_{50}$-H_2P-COF (red curve) had a breakthrough time much longer than that of $[HC{\equiv}C]_{50}$-H_2P-COF (blue curve). Longer breakthrough times are desirable for greater CO_2 capture. For a quantitative evaluation, we arbitrarily chose the required outlet gas purity as <0.05 mol % CO_2. Using this purity specification, we determined the breakthrough times, τ_{break}, for the COFs. Based on the material balance on the absorber, we determined the amount of CO_2 captured during the time interval 0–τ_{break}. Figure 2E shows the

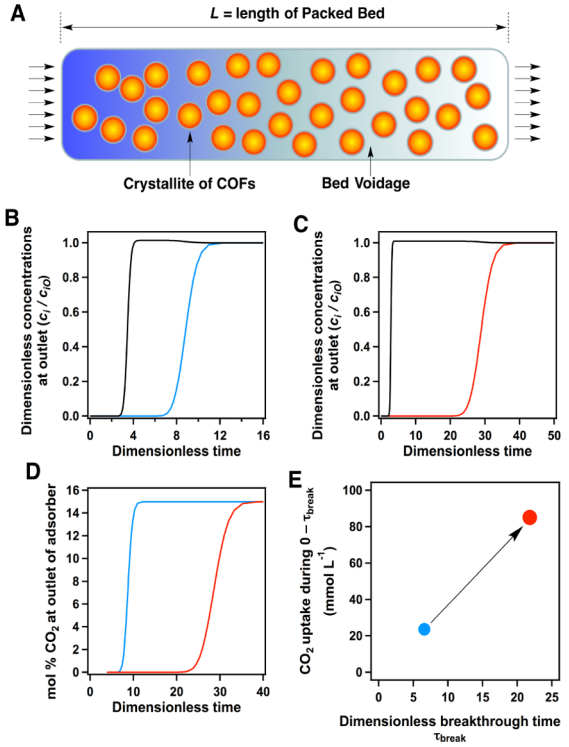

Figure 2. (A) Fixed-bed adsorber for COFs. Flue-gas breakthrough profiles of (B) $[HC{\equiv}C]_{50}$-H_2P-COF and (C) $[EtNH_2]_{50}$-H_2P-COF at 298 K. (D) Comparison of %CO_2 at the adsorber outlet at 298 K (blue curve, $[HC{\equiv}C]_{50}$-H_2P-COF; red curve, $[EtNH_2]_{50}$-H_2P-COF). (E) Comparison of CO_2 capture productivity at 298 K (blue circle, $[HC{\equiv}C]_{50}$-H_2P-COF; red circle, $[EtNH_2]_{50}$-H_2P-COF).

DOI: 10.1021/jacs.5b04300
J. Am. Chem. Soc. 2015, 137, 7079–7082

plot of the number of millimoles of CO_2 capture per liter of adsorbent during the time interval $0 - \tau_{break}$ against the τ_{break}. Notably, $[EtNH_2]_{50}$-H_2P-COF (red circle) exhibited superior CO_2 productivity (90 mmol L^{-1}) compared to $[HC{\equiv}C]_{50}$-H_2P-COF (blue circle; 21 mmol L^{-1}).

COFs with highly functionalized pore wall structures are difficult to obtain via direct polycondensation reactions. The systematic pore surface engineering of COFs enables the tailor-made covalent docking of a variety of different functional groups with controlled loading contents to the pore walls. The surface engineering of the pore walls profoundly affects the surface area, pore size, pore volume, and pore environment. As demonstrated for CO_2 adsorption, pore surface engineering is a high throughput and efficient method for achieving both enhanced adsorption capacities and improved separation capabilities. Notably, this approach is not limited to the present COF and is widely applicable to many other previously reported COFs. We envisage that pore surface engineering might be a general strategy for screening for COF materials that satisfy the multiple requirements of CO_2 capture in industrial-level flow-gas applications.

■ ASSOCIATED CONTENT

Supporting Information

Materials and method, simulations, Tables S1− S5, and Figures S1−S9. The Supporting Information is available free of charge on the ACS Publications website at DOI: 10.1021/jacs.5b04300.

■ AUTHOR INFORMATION

Corresponding Author

*jiang@ims.ac.jp

Notes

The authors declare no competing financial interest.

■ ACKNOWLEDGMENTS

This work was supported by a Grant-in-Aid for Scientific Research (A) (24245030) from MEXT, Japan.

■ REFERENCES

(1) (a) Côté, A. P.; Benin, A. I.; Ockwig, N. W.; O' Keeffe, M.; Matzger, A. J.; Yaghi, O. M. *Science* **2005**, *310*, 1166. (b) Wan, S.; Guo, J.; Kim, J.; Ihee, H.; Jiang, D. *Angew. Chem., Int. Ed.* **2009**, *48*, 5439. (c) Doonan, C. J.; Tranchemontagne, D. J.; Glover, T. G.; Hunt, J. H.; Yaghi, O. M. *Nat. Chem.* **2010**, *2*, 235. (d) DeBlase, C. R.; Silberstein, K. E.; Truong, T.-T.; Abruña, H. D.; Dichtel, W. R. *J. Am. Chem. Soc.* **2013**, *135*, 16821. (e) Bunck, D. N.; Dichtel, W. R. *Angew. Chem., Int. Ed.* **2012**, *51*, 1885. (f) Calik, M.; Auras, F.; Salonen, L. M.; Bader, K.; Grill, I.; Handloser, M.; Medina, D. D.; Dogru, M.; Löbermann, F.; Trauner, D.; Hartschuh, A.; Bein, T. *J. Am. Chem. Soc.* **2014**, *136*, 17802. (g) Ding, S. Y.; Wang, W. *Chem. Soc. Rev.* **2013**, *42*, 548.

(2) (a) Zeng, Y.; Zou, R.; Luo, Z.; Zhang, H.; Yao, X.; Ma, X.; Zou, R.; Zhao, Y. *J. Am. Chem. Soc.* **2015**, *137*, 1020. (b) Medina, D. D.; Rotter, J. M.; Hu, Y.; Dogru, M.; Werner, V.; Auras, F.; Markiewicz, J. T.; Knochel, P.; Bein, T. *J. Am. Chem. Soc.* **2015**, *137*, 1016. (c) Zhou, T.; Xu, S.; Wen, Q.; Pang, Z.; Zhao, X. *J. Am. Chem. Soc.* **2014**, *136*, 15885. (d) Kandambeth, S.; Shinde, D. B.; Panda, M. K.; Lukose, B.; Heine, T.; Banerjee, R. *Angew. Chem., Int. Ed.* **2013**, *52*, 13052. (e) Lanni, L. M.; Tilford, R. W.; Bharathy, M.; Lavigne, J. J. *J. Am. Chem. Soc.* **2011**, *133*, 13975. (f) Uribe-Romo, F. J.; Hunt, J. R.; Furukawa, H.; Klöck, C.; O'Keeffe, M.; Yaghi, O. M. *J. Am. Chem. Soc.* **2009**, *131*, 4570.

(3) (a) Chen, X.; Addicoat, M.; Jin, E.; Zhai, L.; Xu, H.; Huang, N.; Guo, Z.; Liu, L.; Irle, S.; Jiang, D. *J. Am. Chem. Soc.* **2015**, *137*, 3241. (b) Feng, X.; Ding, X.; Jiang, D. *Chem. Soc. Rev.* **2012**, *41*, 6010. (c) Furukawa, H.; Yaghi, O. M. *J. Am. Chem. Soc.* **2009**, *131*, 8875.

(4) (a) Kuhn, P.; Antonietti, M.; Thomas, A. *Angew. Chem., Int. Ed.* **2008**, *47*, 3450. (b) Wang, X.; Maeda, K.; Thomas, A.; Takanabe, K.; Xin, G.; Carlsson, J. M.; Domen, K.; Antonietti, M. *Nat. Mater.* **2008**, *8*, 76. (c) Li, Z.; Feng, X.; Zou, Y.; Zhang, Y.; Xia, H.; Liu, X.; Mu, Y. *Chem. Commun.* **2014**, *50*, 13825. (d) Liu, X.; Guan, C.; Ding, S.; Wang, W.; Yan, H.; Wang, D.; Wan, L. *J. Am. Chem. Soc.* **2013**, *135*, 10470. (e) Nagai, A.; Guo, Z.; Feng, X.; Jin, S.; Chen, X.; Ding, X.; Jiang, D. *Nat. Commun.* **2011**, *2*, 536. (f) Chen, L.; Furukawa, K.; Gao, J.; Nagai, A.; Nakamura, T.; Dong, Y.; Jiang, D. *J. Am. Chem. Soc.* **2014**, *136*, 9806.

(5) (a) Huang, N.; Chen, X.; Krishna, R.; Jiang, D. *Angew. Chem., Int. Ed.* **2015**, *54*, 2986. (b) Xu, H.; Chen, X.; Gao, J.; Lin, J.; Addicoat, M.; Irle, S.; Jiang, D. *Chem. Commun.* **2014**, *50*, 1292.

(6) (a) Spitler, E. L.; Dichtel, W. R. *Nat. Chem.* **2010**, *2*, 672. (b) Colson, J. W.; Woll, A. R.; Mukherjee, A.; Levendorf, M. P.; Spitler, E. L.; Shields, V. B.; Spencer, M. G.; Park, J.; Dichtel, W. R. *Science* **2011**, *332*, 228. (c) Stegbauer, L.; Schwinghammer, K.; Lotsch, B. V. *Chem. Sci.* **2014**, *5*, 2789. (d) Fang, Q.; Zhuang, Z.; Gu, S.; Kaspar, R. B.; Zheng, J.; Wang, J.; Qiu, S.; Yan, Y. *Nat. Commun.* **2014**, *5*, 4503. (e) Rabbani, M. G.; Sekizkardes, A. K.; Kahveci, Z.; Reich, T. E.; Ding, R.; El-Kaderi, H. M. *Chem.—Eur. J.* **2013**, *19*, 3324.

(7) (a) Ding, S. Y.; Gao, J.; Wang, Q.; Zhang, Y.; Song, W.; Su, C.; Wang, W. *J. Am. Chem. Soc.* **2011**, *133*, 19816. (b) Wu, D.; Xu, F.; Sun, B.; Fu, R.; He, H.; Matyjaszewski, K. *Chem. Rev.* **2012**, *112*, 3959. (c) Wu, D.; Li, Z.; Zhong, M.; Kowalewski, T.; Matyjaszewski, K. *Angew. Chem., Int. Ed.* **2014**, *53*, 3957.

(8) (a) Krishna, R.; Long, J. R. *J. Phys. Chem. C* **2011**, *115*, 12941. (b) Mason, J. A.; Sumida, K.; Herm, Z. R.; Krishna, R.; Long, J. R. *Energy Environ. Sci.* **2011**, *4*, 3030.

DOI: 10.1021/jacs.5b04300
J. Am. Chem. Soc. 2015, 137, 7079−7082

Supporting Information

Tailor-Made Pore Surface Engineering in Covalent Organic Frameworks: Systematic Functionalization for Performance Screening

Ning Huang[†], Rajamani Krishna[¶], and Donglin Jiang*[,†]

[†]Department of Materials Molecular Science, Institute for Molecular Science, National Institutes of Natural Sciences, 5-1 Higashiyama, Myodaiji, Okazaki 444-8787, Japan.

[¶]Van't Hoff Institute for Molecular Sciences, University of Amsterdam Science Park 904, 1098 XH Amsterdam, The Netherlands.

E-mail: Jiang@ims.ac.jp

Contents

Section A. Methods

Fourier transform Infrared (FT IR) spectra were recorded on a JASCO model FT IR-6100 infrared spectrometer. UV-Vis-IR diffuse reflectance spectrum (Kubelka-Munk spectrum) was recorded on a JASCO model V-670 spectrometer equipped with integration sphere model IJN-727. Powder X-ray diffraction (PXRD) data were recorded on a Rigaku model RINT Ultima III diffractometer by depositing powder on glass substrate, from $2\theta = 1.5°$ up to 60° with 0.02° increment. Elemental analysis was performed on a Yanako CHN CORDER MT-6 elemental analyzer. Nitrogen sorption isotherms were measured at 77 K with a Bel Japan Inc. model BELSORP-mini II analyzer. Before measurement, the samples were degassed in vacuum at 120 °C for more than 10 h. By using the non-local density functional theory (NLDFT) model, the pore volume was derived from the sorption curve. ^{1}H NMR spectra were recorded on a JEOL model JNM-LA400 NMR spectrometer, where the chemical shifts (δ in ppm) were determined with a residual proton of the solvent as standard.

Section B. Materials and synthetic procedures

n-Butanol, *o*-dichlorobenzene (*o*-DCB), anhydrous acetone (99.5%), and tetrahydrofuran were purchased from Wako Chemicals. 1,4-Phthalaldehyde (PA) was purchased from TCI. Free-base 5,10,15,20-tetrakis(*p*-tetraphenylamino) porphyrin (H_2P) was prepared from *p*-nitrobenzaldehyde using a literature procedure.[S1] 2,5-Dihydroxyterephthalaldehyde (DHTA) and 2,5-bis(2-propynyloxy) terephthalaldehyde (BPTA) were synthesized according to a reported method.[S2,S3]

$[HC\equiv C]_X$-H_2P-COFs. An *o*-DCB/BuOH (0.5 mL / 0.5 mL) mixture of H_2P (0.022 mmol, 14.9 mg) and DHTA/BPTA (total 0.044 mmol) at different molar ratios of 100/0, 75/25, 50/50, 25/75, and 0/100 in the presence of acetic acid catalyst (3 M, 0.1 mL) in a Pyrex tube (10 mL) was degassed by three freeze–pump–thaw cycles. The tube was sealed off by flame and heated at 120 °C for 3 days. The precipitate was collected via centrifuge, washed with THF for 6 times, and washed with acetone 3 times. The powder was dried at 120 °C under vacuum overnight to give the corresponding COFs in isolated yields of 80%, 72%, 69%, 86%, and 80% for the $[HC\equiv C]_0$-H_2P-COF, $[HC\equiv C]_{25}$-H_2P-COF, $[HC\equiv C]_{50}$-H_2P-COF, $[HC\equiv C]_{75}$-H_2P-COF, and $[HC\equiv C]_{100}$-H_2P-COF, respectively.

$[R]_X$-H_2P-COFs. A toluene/*n*-butanol (0.8 mL / 0.2 mL) mixture of $[HC\equiv C]_{25}$-H_2P-COF (20 mg) in the presence of CuI (2 mg) and DIPEA (40 μL) in a Pyrex tube (10 mL) was added with azide compounds. The tube was degassed via three freeze–pump–thaw cycles and the mixture was stirred at room temperature for 24 h. The precipitate was collected via centrifuge, washed with ethanol 5 times, and dried at room temperature under vacuum, to produce $[R]_{25}$-H_2P-COF as a deep brown solid in quantitative yield. The ethynyl groups were quantatively reacted with the azide units as evident by the IR spectra. The click reaction of $[HC\equiv C]_X$-H_2P-COFs (X = 50, 75, and 100) with azides compounds were performed according to this method under otherwise same conditions.

Section C. Fitting of pure component isotherms

The salient properties of two different COFs ($[HC\equiv C]_{25\%}$-H_2PCOF and $[EtNH_2]_{25\%}$-H_2PCOF) are specified in Table 1. The potential of these COFs are evaluated for the separation of CO_2/N_2 mixtures that is relevant for CO_2 capture from flue gases. For our evaluations, we assume the CO_2/N_2 mixtures to contain 15% CO_2, and 85% N_2, following the earlier work of Mason et al.[S4]

The experimentally measured excess loadings of CO_2, and N_2, obtained at different temperatures, were first converted to absolute loadings before data fitting. The procedure for converting to absolute loadings is the same as described in the Supporting Information accompanying the paper of Wu et al.[S5] For the purpose of converting to absolute loadings, the pore volumes used are specified in Table S4. The isotherm data for CO_2 were fitted with the 1-site Langmuir model:

$$q = q_{sat}\frac{bp}{1+bp} \qquad (1)$$

with T-dependent parameter b

$$b_A = b_0 \exp\left(\frac{E}{RT}\right) \qquad (2)$$

The 1-site Langmuir T-dependent parameters for adsorption of CO_2 are provided in Table S5. Table S6 provides the T-dependent Langmuir parameters for N_2 in different materials.

Section D. Isosteric heat of adsorption

The isosteric heat of adsorption, Q_{st}, defined as

$$Q_{st} = RT^2 \left(\frac{\partial \ln p}{\partial T} \right)_q \qquad (3)$$

was determined using the pure component isotherm fits using the Clausius-Clapeyron equation. The Q_{st} values are summarized in Table S2.

Section E. IAST calculations

The selectivity of preferential adsorption of component 1 over component 2 in a mixture containing 1 and 2, perhaps in the presence of other components too, can be formally defined as

$$S_{ads} = \frac{q_1/q_2}{p_1/p_2} \qquad (4)$$

In equation (4), q_1 and q_2 are the *absolute* component loadings of the adsorbed phase in the mixture. These component loadings are also termed the uptake capacities. In all the calculations to be presented below, the calculations of q_1 and q_2 are based on the use of the Ideal Adsorbed Solution Theory (IAST) of Myers and Prausnitz.[S6] The accuracy of the IAST calculations for estimation of the component loadings for several binary mixtures in a wide variety of zeolites, and MOFs has been established by comparison with Configurational-Bias Monte Carlo (CBMC) simulations of mixture adsorptions.[S7-S12]

The IAST calculations of the component uptakes for 15/85 CO_2/N_2 mixtures at 198 K are shown in Figure S9a and S9b.

Section F. Simulation methodology for transient breakthrough in fixed bed absorbers

The separation of CO_2/N_2 mixtures is commonly carried out in fixed bed absorbers in which the separation performance is dictated by a combination of three separate factors: (a) adsorption selectivity, (b) uptake capacity, and (c) intra-crystalline diffusivities of guest molecules within the pores. Transient breakthrough simulations are required for a proper evaluation of MOFs; the simulation methodology used in our work is described in earlier publications.[S13,S14] A brief summary of the simulation methodology is presented below.

Assuming plug flow of an *n*-component gas mixture through a fixed bed maintained under isothermal conditions (see schematic in Figure 4a), the partial pressures in the gas phase at any position and instant of time are obtained by solving the following set of partial differential equations for each of the species *i* in the gas mixture.[S12]

$$\frac{1}{RT}\frac{\partial p_i(t,z)}{\partial t} = -\frac{1}{RT}\frac{\partial\left(v(t,z)p_i(t,z)\right)}{\partial z} - \frac{\left(1-\varepsilon\right)}{\varepsilon}\rho\frac{\partial \bar{q}_i(t,z)}{\partial t}; \qquad i = 1,2,\ldots n \qquad (5)$$

In equation (5), t is the time, z is the distance along the adsorber, r is the framework density, e is the bed voidage, v is the interstitial gas velocity, and $\bar{q}_i(t,z)$ is the *spatially averaged* molar loading within the crystallites of radius r_c, monitored at position z, and at time t.

At any time t, during the transient approach to thermodynamic equilibrium, the spatially averaged molar loading within the crystallite r_c is obtained by integration of the radial loading profile

$$\bar{q}_i(t) = \frac{3}{r_c^3}\int_0^{r_c} q_i(r,t)r^2 dr \qquad (6)$$

For transient unary uptake within a crystal at any position and time with the fixed bed, the radial distribution of molar loadings, q_i, within a spherical crystallite, of radius r_c, is obtained from a solution of a set of differential equations describing the uptake

$$\frac{\partial q_i(r,t)}{\partial t} = -\frac{1}{\rho}\frac{1}{r^2}\frac{\partial}{\partial r}\left(r^2 N_i\right) \qquad (7)$$

The molar flux N_i of component *i* is described by the simplified version of the Maxwell-Stefan equations in which both correlation effects and thermodynamic coupling effects are considered to be of negligible importance[S15]

$$N_i = -\rho D_i\frac{\partial q_i}{\partial r} \qquad (8)$$

Summing equation (**6**) over all *n* species in the mixture allows calculation of the *total average* molar loading of the mixture within the crystallite

$$\bar{q}_t(t,z) = \sum_{i=1}^{n} \bar{q}_i(t,z) \qquad (9)$$

The *interstitial* gas velocity is related to the *superficial* gas velocity by

$$v = \frac{u}{\varepsilon} \qquad (10)$$

In industrial practice, the most common operation uses a step-wise input of mixtures to be separated into an absorber bed that is initially free of adsorbents, i.e. we have the initial condition

$$t = 0; \quad q_i(0,z) = 0 \qquad (11)$$

At time $t = 0$, the inlet to the absorber, $z = 0$, is subjected to a step input of the *n*-component gas mixture and this step input is maintained till the end of the adsorption cycle when steady-state conditions are reached.

$$t \geq 0; \quad p_i(0,t) = p_{i0}; \quad u(0,t) = u_0 \qquad (12)$$

where u_0 is the superficial gas velocity at the inlet to the absorber.

The breakthrough characteristics for any component is essentially dictated by two sets of parameters: (a) The characteristic contact time $\frac{L}{v} = \frac{L\varepsilon}{u}$ between the crystallites and the surrounding fluid phase, and (b) $\frac{D_i}{r_c^2}$, that reflect the importance of intra-crystalline diffusion limitations. It is common to use the dimensionless time, $\tau = \frac{tu}{L\varepsilon}$, obtained by dividing the actual time *t*, by the characteristic time, $\frac{L\varepsilon}{u}$ when plotting simulated breakthrough curves.[S14]

If the value of $\frac{D_i}{r_c^2}$ is large enough to ensure that intra-crystalline gradients are absent and the entire crystallite particle can be considered to be in thermodynamic equilibrium with the surrounding bulk gas phase at that time *t*, and position *z* of the adsorber

$$\bar{q}_i(t,z) = q_i(t,z) \qquad (13)$$

The molar loadings at the *outer surface* of the crystallites, i.e. at $r = r_c$, are calculated on the basis of adsorption equilibrium with the bulk gas phase partial pressures p_i at that position *z* and time *t*. The adsorption equilibrium can be calculated on the basis of the IAST. The assumption of

thermodynamic equilibrium at every position z, and any time t, i.e. invoking Equation (13), generally results in sharp breakthroughs for each component. Sharp breakthroughs are desirable in practice because this would result in high productivity of pure products. Essentially, the influence of intra-crystalline diffusion is to reduce the productivity of pure gases. For all the breakthrough calculations reported in this work, we assume negligible diffusion resistances for all materials and we invoke the simplified Equation (13).

Section G. Notation

b_A dual-Langmuir-Freundlich constant for species *i* at adsorption site A, $Pa^{-\nu_i}$

c_i molar concentration of species *i* in gas mixture, mol m^{-3}

c_{i0} molar concentration of species *i* in gas mixture at inlet to adsorber, mol m^{-3}

L length of packed bed adsorber, m

N number of species in the mixture, dimensionless

N_i molar flux of species *i*, mol m^{-2} s^{-1}

p_i partial pressure of species *i* in mixture, Pa

p_t total system pressure, Pa

q_i component molar loading of species *i*, mol kg^{-1}

$\bar{q}_i(t)$ *spatially averaged* component molar loading of species *i*, mol kg^{-1}

r_c radius of crystallite, m

R gas constant, 8.314 J mol^{-1} K^{-1}

t time, s

T absolute temperature, K

u superficial gas velocity in packed bed, m s^{-1}

v interstitial gas velocity in packed bed, m s^{-1}

Greek letters

e voidage of packed bed, dimensionless

r framework density, kg m^{-3}

τ time, dimensionless

Subscripts

i referring to component

i_{break} referring to breakthrough

t referring to total mixture

Section H. Supporting Tables

Table S1. Elemental analysis results of $[HC{\equiv}C]_X$-H_2P-COFs and $[R]_X$-H_2P-COFs.

COFs		C%	H%	N%
$[HC{\equiv}C]_0$-H_2P-COF	Calcd.	76.95	4.25	11.97
	Found	77.36	4.88	10.87
$[HC{\equiv}C]_{25}$-H_2P-COF	Calcd.	77.76	4.14	11.52
	Found	76.86	4.63	10.92
$[HC{\equiv}C]_{50}$-H_2P-COF	Calcd.	78.4	4.19	11.08
	Found	76.92	4.84	10.87
$[HC{\equiv}C]_{75}$-H_2P-COF	Calcd.	78.99	4.22	10.68
	Found	77.23	4.92	9.41
$[HC{\equiv}C]_{100}$-H_2P-COF	Calcd.	79.54	4.26	10.31
	Found	77.92	4.86	9.62
$[Et]_{25}$-H_2P-COF	Calcd.	80.95	4.25	10.43
	Found	78.96	4.82	9.21
$[Et]_{50}$-H_2P-COF	Calcd.	81.29	4.13	11.17
	Found	78.76	5.02	9.97
$[Et]_{75}$-H_2P-COF	Calcd.	81.87	4.02	11.24
	Found	79.34	4.67	11.22
$[Et]_{100}$-H_2P-COF	Calcd.	82.11	3.85	11.61
	Found	78.82	4.62	10.79
$[EtOH]_{25}$-H_2P-COF	Calcd.	74.05	4.37	10.79
	Found	72.42	4.66	9.46
$[EtOH]_{50}$-H_2P-COF	Calcd.	71.76	4.34	9.85
	Found	69.92	4.68	8.88
$[EtOH]_{75}$-H_2P-COF	Calcd.	69.84	4.31	9.05
	Found	68.74	4.88	8.34
$[EtOH]_{100}$-H_2P-COF	Calcd.	68.21	4.29	8.37
	Found	64.43	5.17	7.02
$[EtNH_2]_{25}$-H_2P-COF	Calcd.	72.25	4.32	11.68

	Found	70.86	5.01	9.74
$[EtNH_2]_{50}$-H_2P-COF	Calcd.	71.77	4.24	11.86
	Found	70.26	5.27	9.89
$[EtNH_2]_{75}$-H_2P-COF	Calcd.	71.53	4.16	12.02
	Found	69.15	5.26	10.64
$[EtNH_2]_{100}$-H_2P-COF	Calcd.	71.34	4.09	12.34
	Found	69.75	5.17	11.24
$[MeOAc]_{25}$-H_2P-COF	Calcd.	77.94	4.32	11.38
	Found	75.43	5.02	10.62
$[MeOAc]_{50}$-H_2P-COF	Calcd.	77.34	4.26	11.02
	Found	75.74	4.89	9.74
$[MeOAc]_{75}$-H_2P-COF	Calcd.	76.95	4.18	10.92
	Found	74.76	5.02	9.03
$[MeOAc]_{100}$-H_2P-COF	Calcd.	76.69	4.13	10.77
	Found	74.68	5.37	9.74
$[AcOH]_{25}$-H_2P-COF	Calcd.	81.36	4.32	10.86
	Found	79.52	5.16	9.64
$[AcOH]_{50}$-H_2P-COF	Calcd.	80.11	3.91	10.61
	Found	78.31	5.03	9.61
$[AcOH]_{75}$-H_2P-COF	Calcd.	78.46	3.76	10.42
	Found	76.34	4.36	9.44
$[AcOH]_{100}$-H_2P-COF	Calcd.	75.77	3.34	10.23
	Found	73.61	4.71	9.52

Table S2. Porosity, CO_2 uptake, and Q_{st} value of $[HC{\equiv}C]_X$-H_2P-COFs and $[R]_X$-H_2P-COFs.

COFs	S_{BET} ($m^2\ g^{-1}$)	Pore size (nm)	Pore volume ($cm^3\ g^{-1}$)	CO_2 uptake ($mg\ g^{-1}$)		Q_{st} ($kJ\ mol^{-1}$)
				273 K	298 K	
$[C{\equiv}C]_0$-H_2P-COF	1474	2.5	0.75	72	38	17.2
$[C{\equiv}C]_{25}$-H_2P-COF	1431	2.3	0.71	54	29	16.8
$[C{\equiv}C]_{50}$-H_2P-COF	962	2.1	0.57	48	26	16.5
$[C{\equiv}C]_{75}$-H_2P-COF	683	1.9	0.42	43	24	15.7
$[C{\equiv}C]_{100}$-H_2P-COF	426	1.6	0.28	39	20	15.3
$[Et]_{25}$-H_2P-COF	1326	2.2	0.55	55	29	15.5
$[Et]_{50}$-H_2P-COF	821	1.9	0.48	46	25	15.3
$[Et]_{75}$-H_2P-COF	485	1.6	0.34	41	23	15.6
$[Et]_{100}$-H_2P-COF	187	1.5	0.18	38	21	15.3
$[MeOAc]_{25}$-H_2P-COF	1238	2.1	0.51	84	42	16.4
$[MeOAc]_{50}$-H_2P-COF	754	1.8	0.42	88	47	17.1
$[MeOAc]_{75}$-H_2P-COF	472	1.5	0.31	82	42	16.7
$[MeOAc]_{100}$-H_2P-COF	156	1.1	0.14	65	34	17.8
$[AcOH]_{25}$-H_2P-COF	1252	2.2	0.52	94	50	17.7
$[AcOH]_{50}$-H_2P-COF	866	1.8	0.45	117	64	17.8
$[AcOH]_{75}$-H_2P-COF	402	1.5	0.32	109	58	18.3
$[AcOH]_{100}$-H_2P-COF	186	1.3	0.18	96	50	18.8
$[EtOH]_{25}$-H_2P-COF	1248	2.2	0.56	92	50	18.2
$[EtOH]_{50}$-H_2P-COF	784	1.9	0.43	124	71	19.7
$[EtOH]_{75}$-H_2P-COF	486	1.6	0.36	117	63	19.2
$[EtOH]_{100}$-H_2P-COF	214	1.4	0.19	84	44	19.3
$[EtNH_2]_{25}$-H_2P-COF	1402	2.2	0.58	116	60	20.4

$[EtNH_2]_{50}$-H_2P-COF	1044	1.9	0.50	133	67	20.9
$[EtNH_2]_{75}$-H_2P-COF	568	1.6	0.36	157	82	20.8
$[EtNH_2]_{100}$-H_2P-COF	382	1.3	0.21	97	52	20.9

Table S3. Salient properties of $[HC{\equiv}C]_{50}$-H_2P-COF and $[EtNH_2]_{50}$-H_2P-COF (The crystal framework densities, required in the breakthrough simulations, are estimated as (bulk density)/(one-bed porosity) with the assumption that the bed porosity is 0.4.).

COFs	Bulk density ($g\ cm^{-3}$)	S_{BET} ($m^2\ g^{-1}$)	Pore volume ($cm^3\ g^{-1}$)	Pore size (nm)
$[HC{\equiv}C]_{50}$-H_2P-COF	0.24	683	0.42	1.91
$[EtNH_2]_{50}$-H_2P-COF	0.27	568	0.36	1.56

Table S4. One-site Langmuir parameters for adsorption of CO_2 in COFs (The experimentally measured excess loadings were first converted to absolute loadings before data fitting.).

COFs	q_{sat} ($mol\ kg^{-1}$)	b_0 (Pa^{-v})	E ($kJ\ mol^{-1}$)
$[HC{\equiv}C]_{50}$-H_2P-COF	18	3.82×10^{-10}	16.5
$[EtNH_2]_{50}$-H_2P-COF	15	3.14×10^{-10}	20.9

Table S5. One-site Langmuir parameters for N_2 in different materials.

COFs	$q_{A,sat}$ ($mol\ kg^{-1}$)	b_{A0} (Pa^{-1})	E_A ($kJ\ mol^{-1}$)
$[HC{\equiv}C]_{50}$-H_2P-COF	2	3.28×10^{-9}	13.8
$[EtNH_2]_{50}$-H_2P-COF	2	8.4×10^{-09}	11

Section I. Supporting Figures.

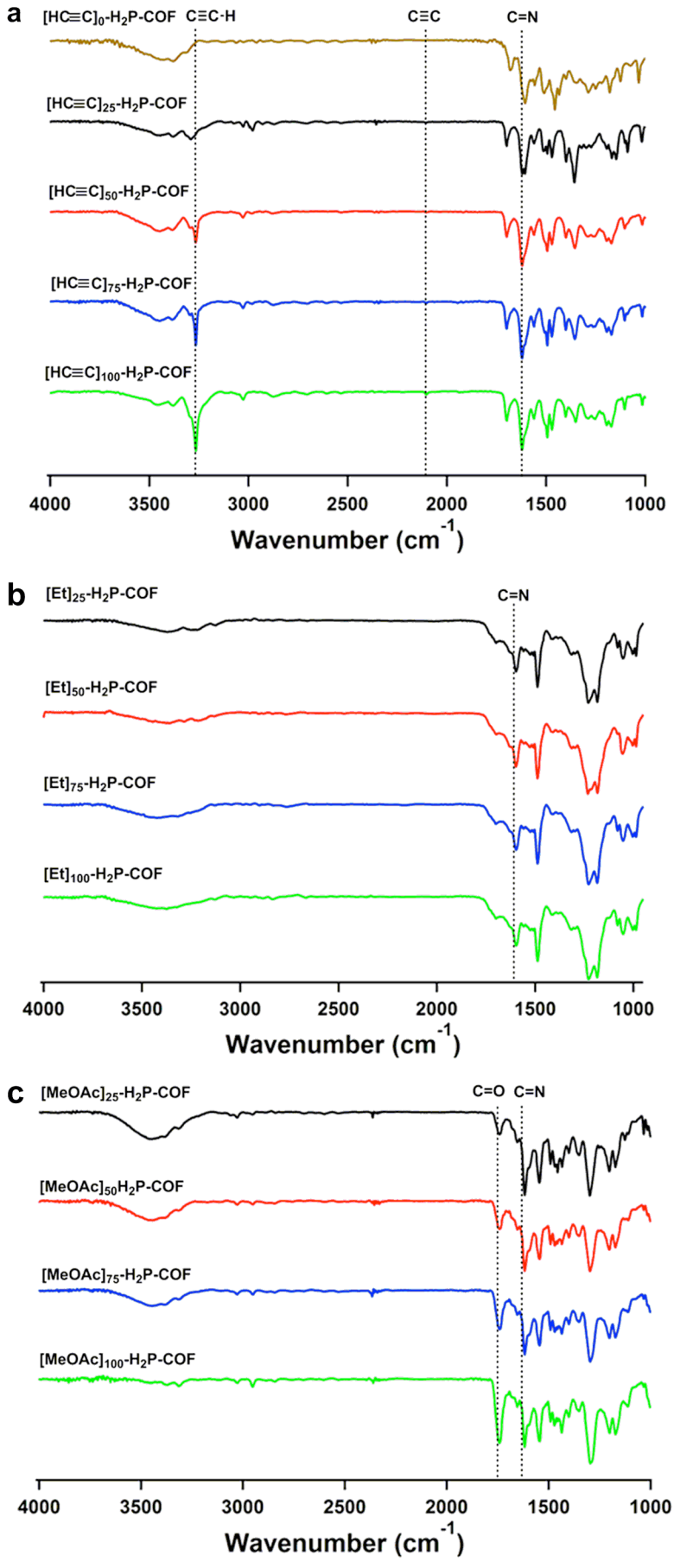

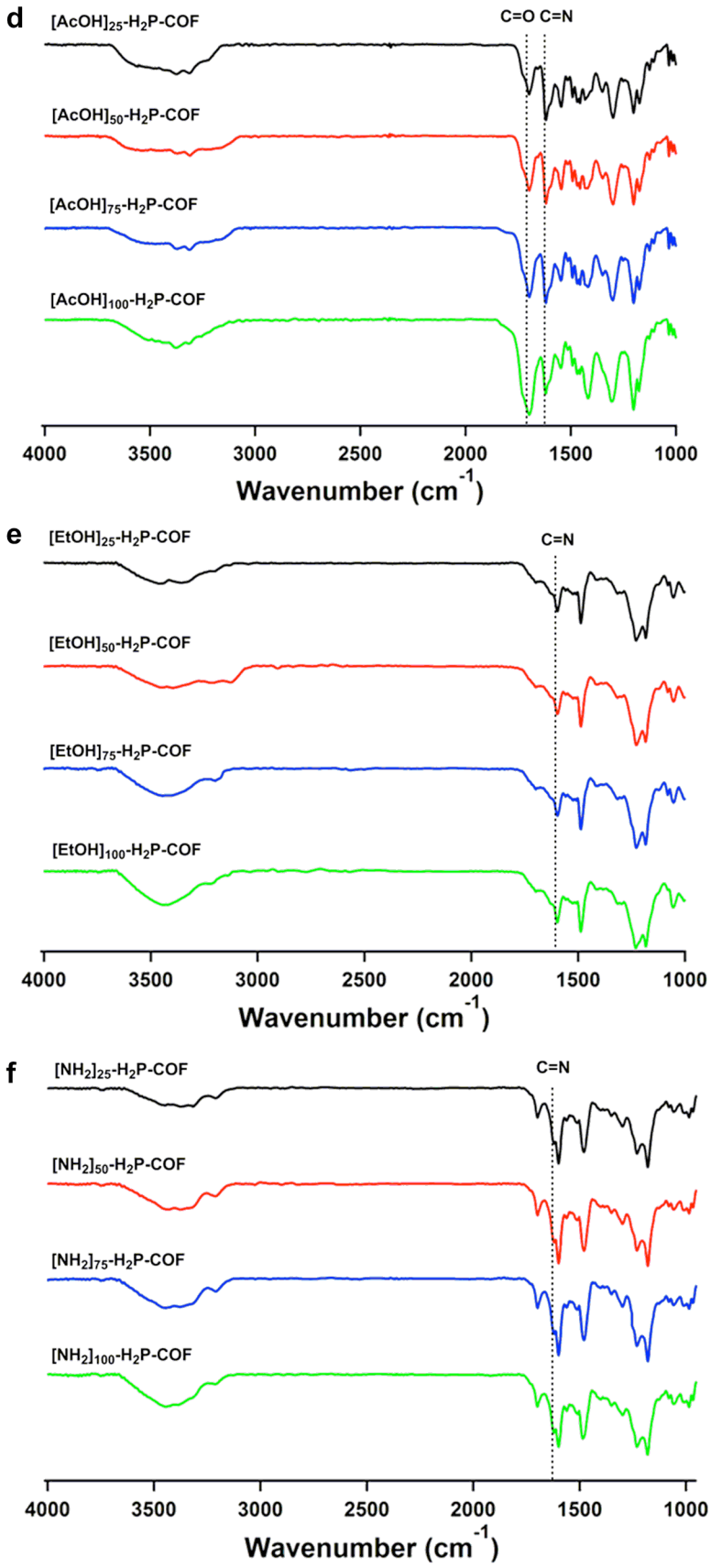

Figure S1. FT-IR spectra of $[HC{\equiv}C]_X$-H_2P-COFs, $[Et]_X$-H_2P-COFs, $[MeOAc]_X$-H_2P-COFs, $[AcOH]_X$-H_2P-COFs, $[EtOH]_X$-H_2P-COFs and $[EtNH_2]_X$-H_2P-COFs (X = 0, 25, 50, 75, and 100).

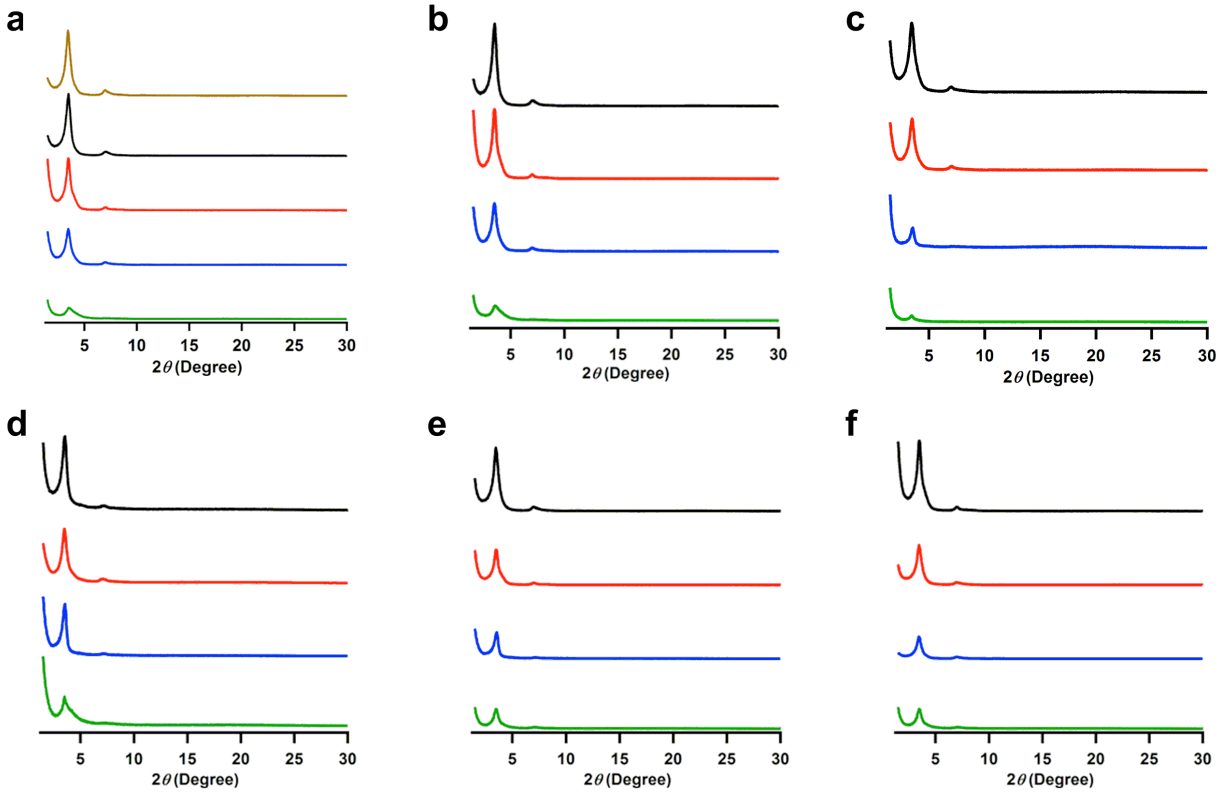

Figure S2. The XRD patterns of (**a**) $[HC{\equiv}C]_X$-H_2P-COFs, (**b**) $[Et]_X$-H_2P-COFs, (**c**) $[MeOAc]_X$-H_2P-COFs, (**d**) $[AcOH]_X$-H_2P-COFs, (**e**) $[EtOH]_X$-H_2P-COFs, and (**f**) $[EtNH_2]_X$-H_2P-COFs (orange : X = 0, black: X = 25, red: X = 50, blue: X = 75, and green: X = 100).

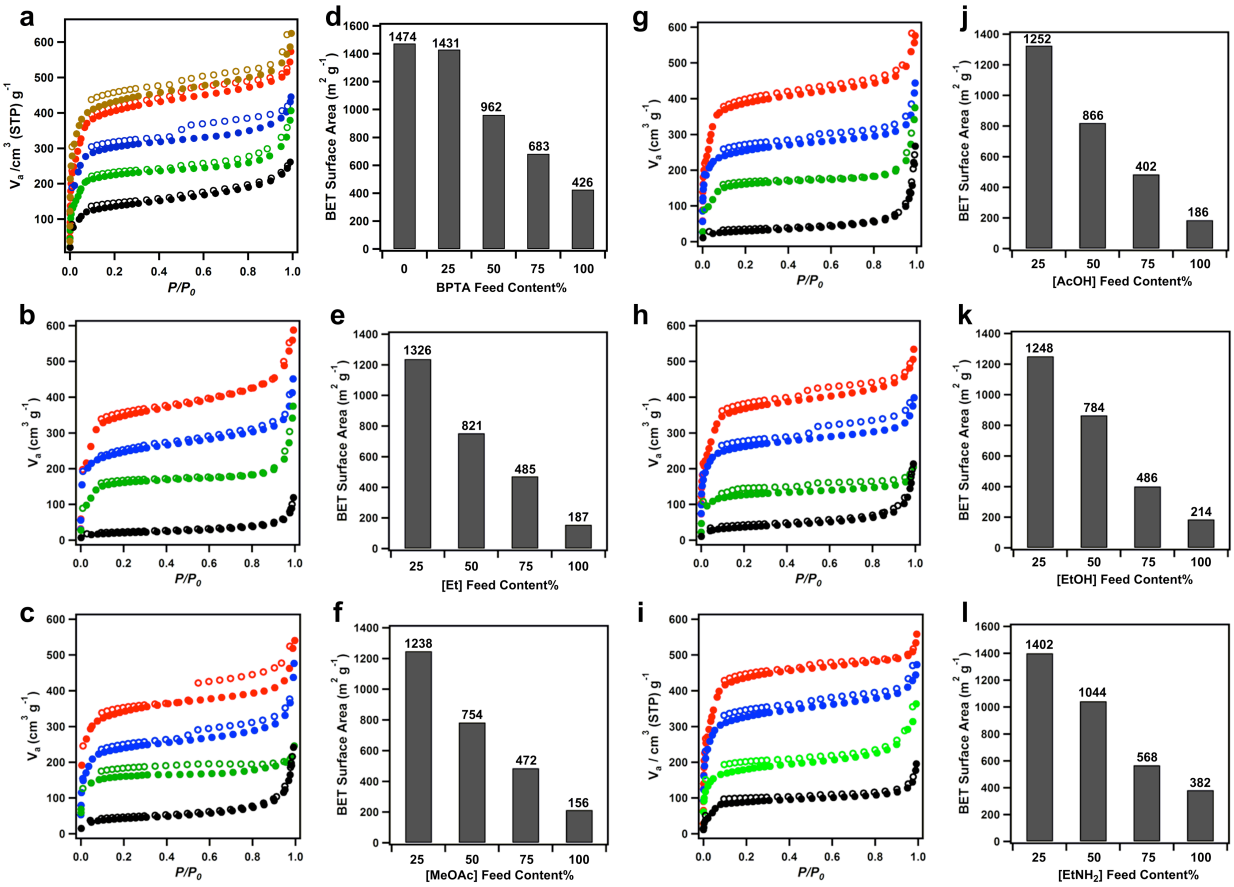

Figure S3. Nitrogen sorption isotherm curves of (**a**) $[HC{\equiv}C]_X$-H_2P-COFs, (**b**)$[Et]_X$-H_2P-COFs, (**c**) $[MeOAc]_X$-H_2P-COFs, (**g**) $[AcOH]_X$-H_2P-COFs, (**h**) $[EtOH]_X$-H_2P-COFs, and (**i**) $[EtNH_2]_X$-H_2P-COFs at 77K (orange: X =0, red: X = 25, blue: X = 50, green: X = 75, black: X = 100). BET surface areas of (**d**) $[HC{\equiv}C]_X$-H_2P-COFs, (**e**)$[Et]_X$-H_2P-COFs, (**f**) $[MeOAc]_X$-H_2P-COFs, (**j**) $[AcOH]_X$-H_2P-COFs, (**k**) $[EtOH]_X$-H_2P-COFs, and (**l**) $[EtNH_2]_X$-H_2P-COFs.

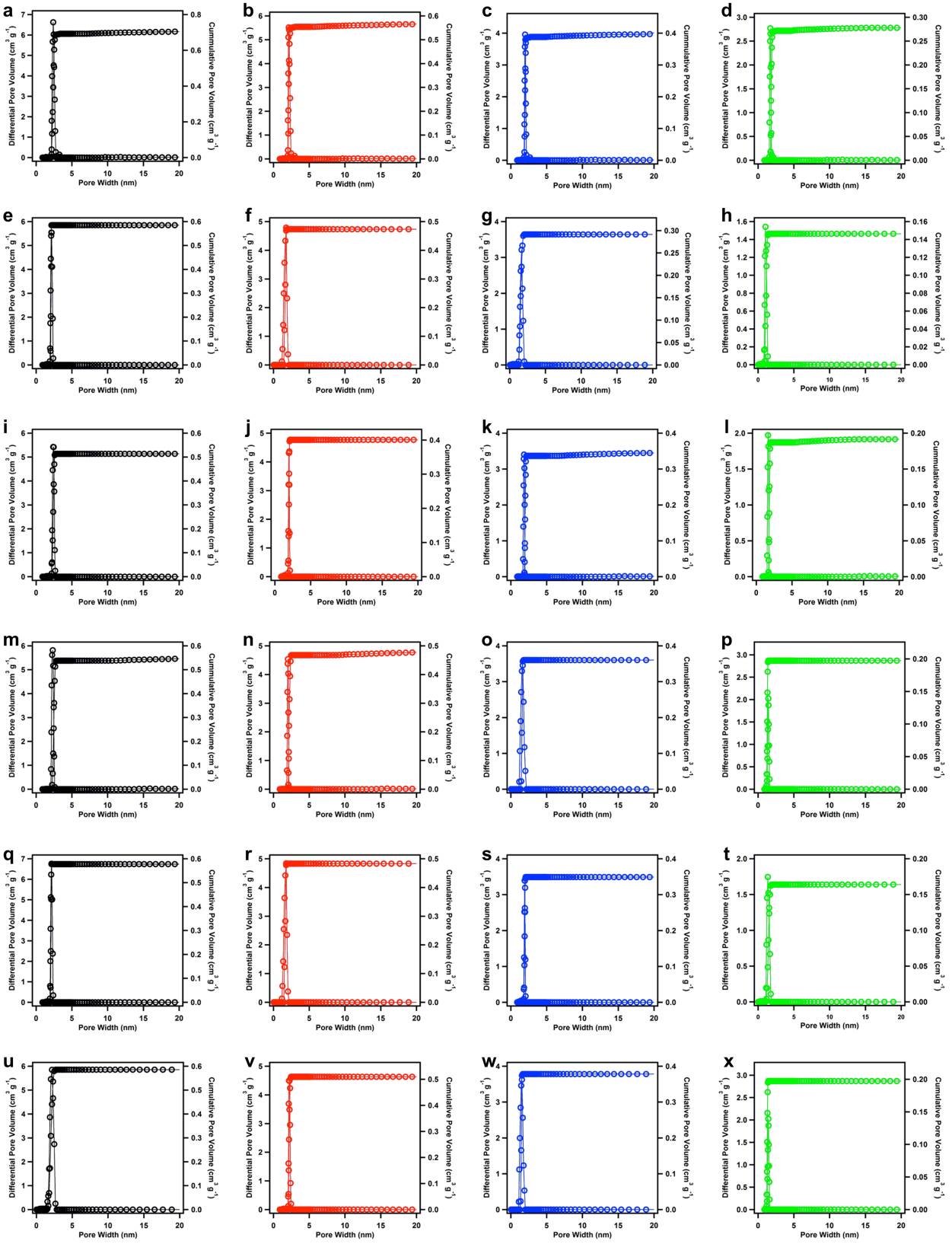

Figure S4. Pore size and pore volume distribution files for (**a-d**) $[HC{\equiv}C]_X$-H_2P-COFs, (**e-h**) $[Et]_X$-H_2P-COFs, (**i-l**) $[MeOAc]_X$-H_2P-COFs, (**m-p**) $[AcOH]_X$-H_2P-COFs, (**q-t**) $[EtOH]_X$-H_2P-COFs, and (**u-x**) $[EtNH_2]_X$-H_2P-COFs (from left to right, X = 25, 50, 75, and 100).

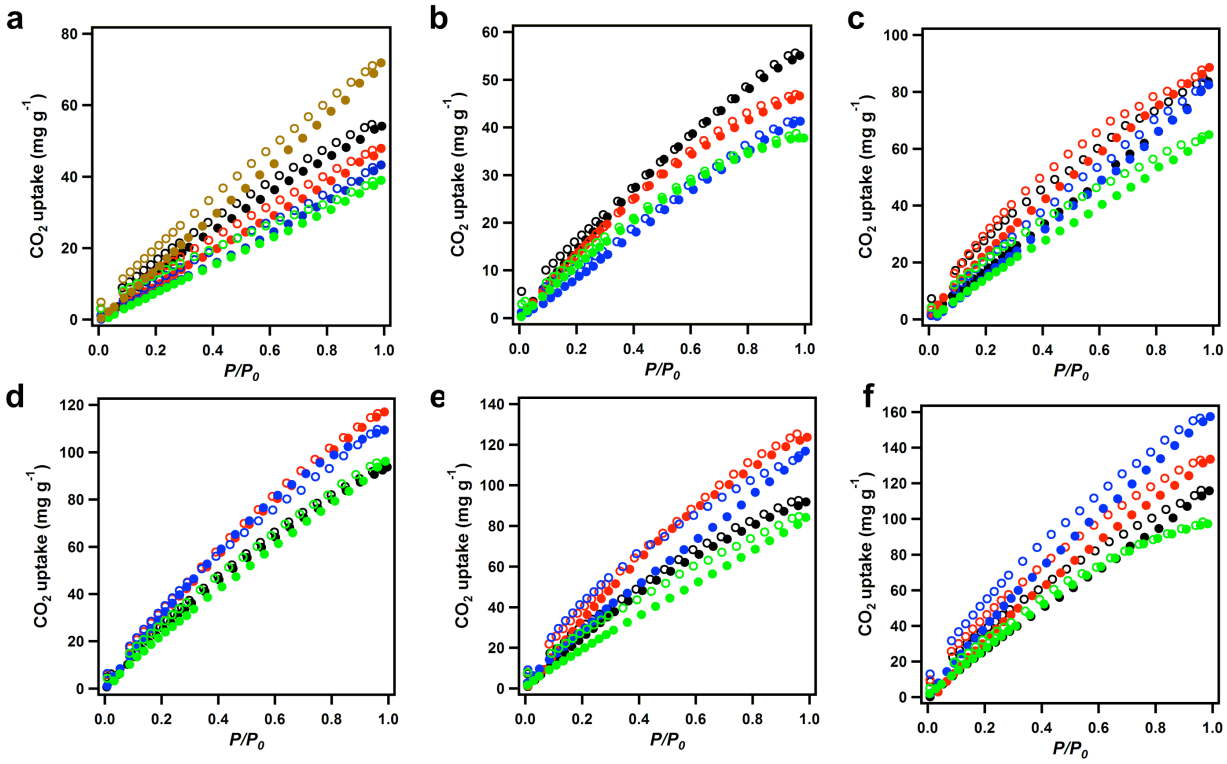

Figure S5. CO_2 sorption curves of (**a**) $[HC{\equiv}C]_X$-H_2P-COFs, (**b**) $[Et]_X$-H_2P-COFs, (**c**) $[MeOAc]_X$-H_2P-COFs, (**d**) $[AcOH]_X$-H_2P-COFs, (**e**) $[EtOH]_X$-H_2P-COFs, and (**f**) $[EtNH_2]_X$-H_2P-COFs at 273 K (orange: X =0, black: X = 25, red: X = 50, blue: X = 75, green: X = 100).

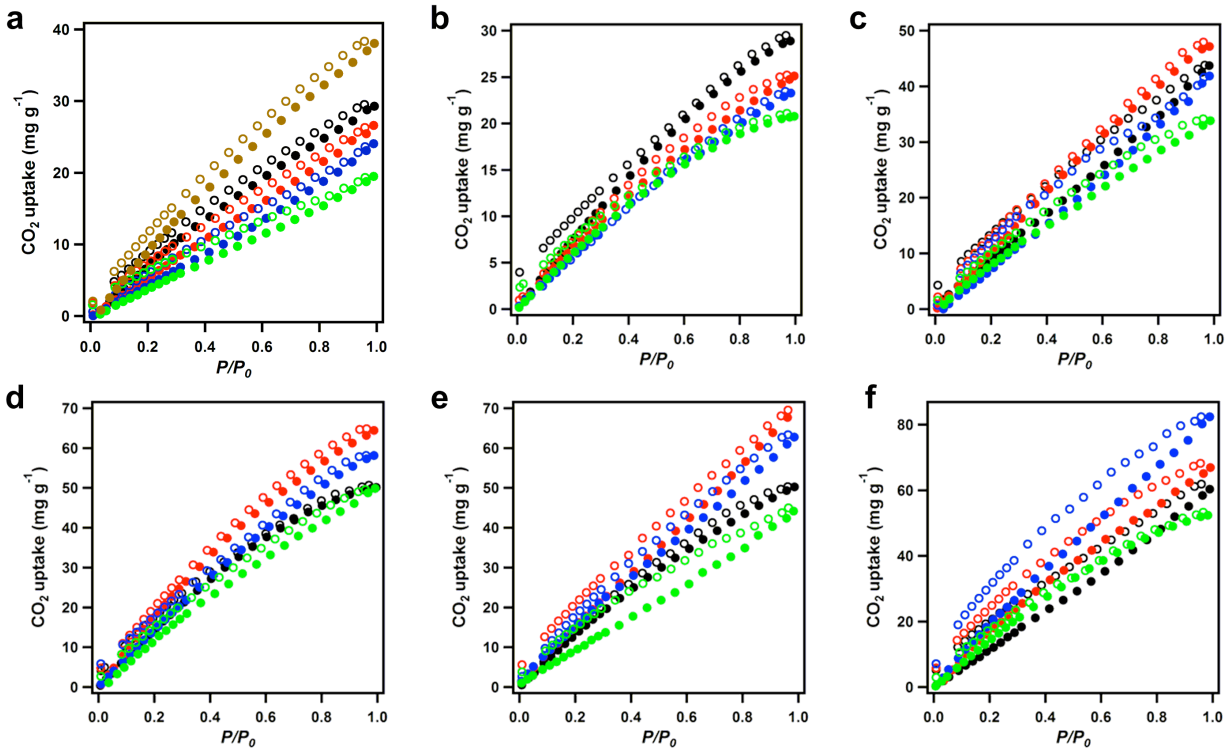

Figure S6. CO_2 sorption curves of (**a**) $[HC{\equiv}C]_X$-H_2P-COFs, (**b**) $[Et]_X$-H_2P-COFs, (**c**) $[MeOAc]_X$-H_2P-COFs, (**d**) $[AcOH]_X$-H_2P-COFs, (**e**) $[EtOH]_X$-H_2P-COFs, and (**f**) $[EtNH_2]_X$-H_2P-COFs at 298 K (orange: X =0, black: X = 25, red: X = 50, blue: X = 75, green: X = 100).

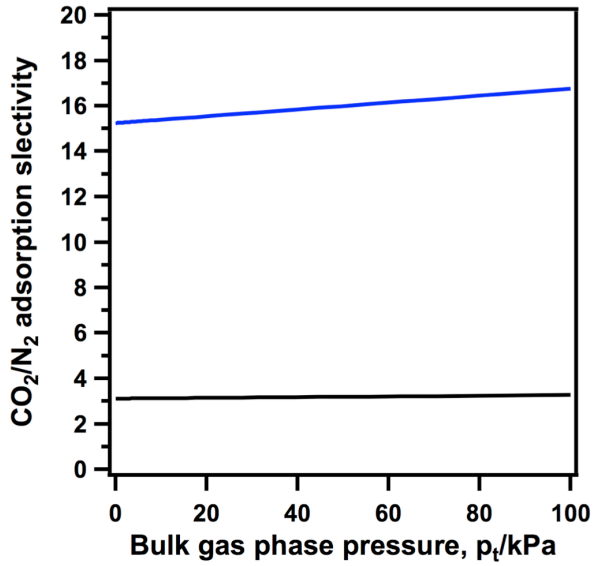

Figure S7. Calculations using Ideal Adsorbed Solution Theory (IAST) of Myers and Prausnitz[6] for CO_2/N_2 adsorption selectivity for a binary CO_2/N_2 gas mixture maintained at isothermal conditions at 298 K. In these calculations the partial pressures of CO_2 and N_2 are taken to be p_1/p_2=15/85 (blue: $[EtNH_2]_{50}$-H_2P-COF; black: $[HC{\equiv}C]_{50}$-H_2P-COF).

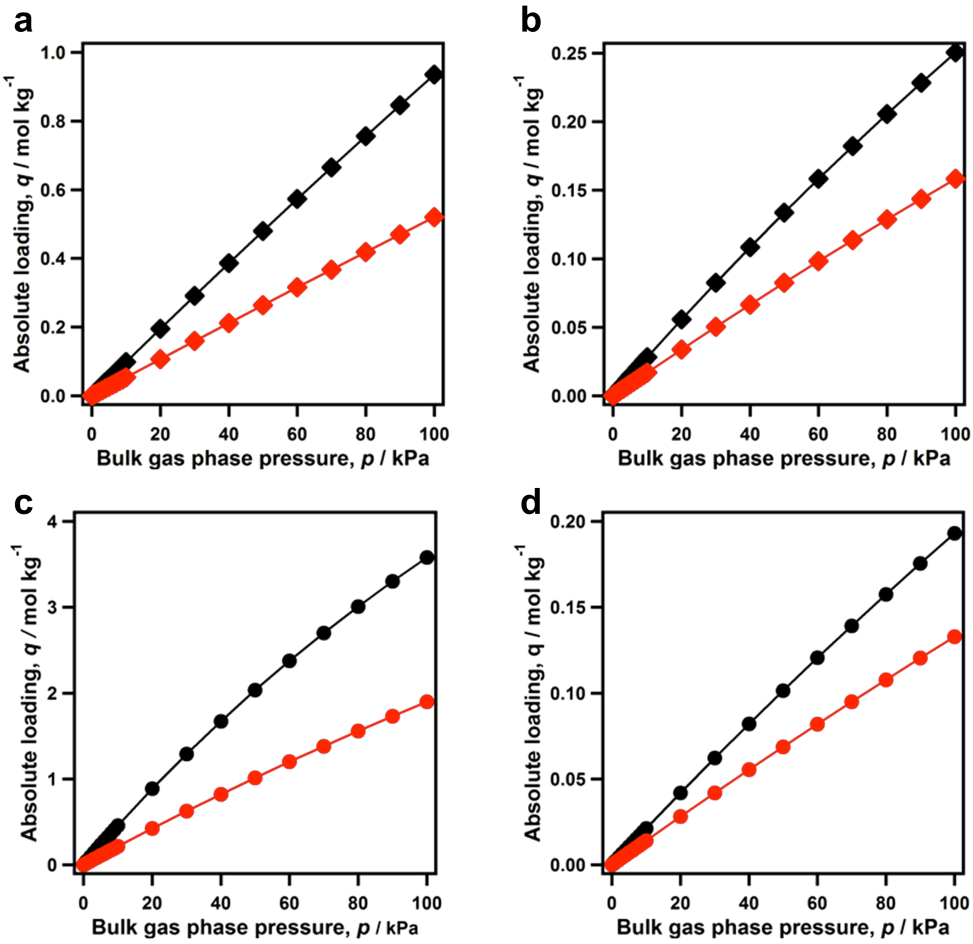

Figure S8. The fitted CO_2 (**a** and **c**) and N_2 (**b** and **d**) isotherm curves (black: 273K, red: 298K) of (**a**, **b**) $[HC{\equiv}C]_{50}$-H_2P-COF and (**c**, **d**) $[EtNH_2]_{50}$-H_2P-COF.

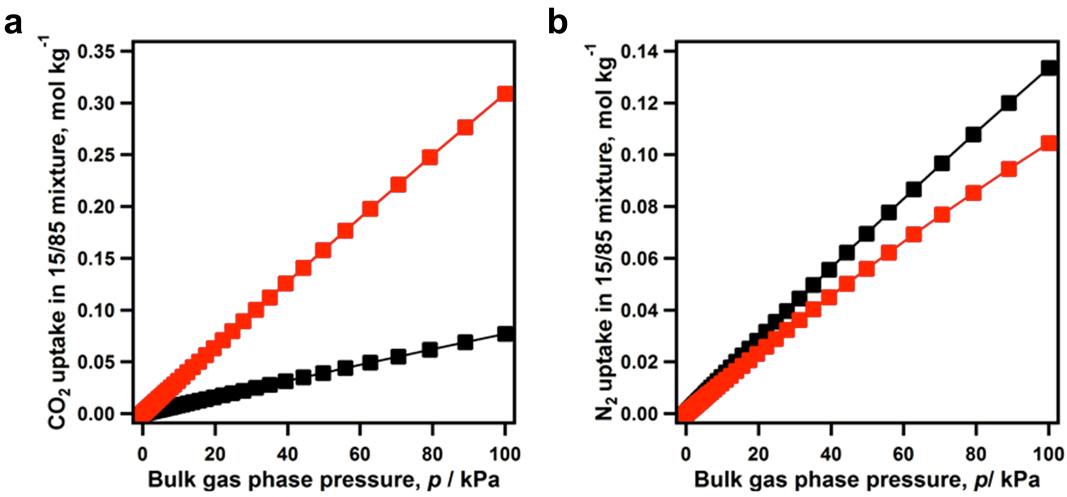

Figure S9. Calculations using ideal adsorbed solution theory (IAST) of Myers and Prausnitz for uptakes of CO_2 and N_2, expressed as moles per kg of adsorbent, in equilibrium with a binary CO_2/N_2 gas mixture maintained at isothermal conditions at 298 K (black: $[HC{\equiv}C]_{50}$-H_2P-COF, red: $[EtNH_2]_{50}$-H_2P-COF) . In these calculations the partial pressures of CO_2 and N_2 are taken to be $p_1/\ p_2$=15/85.

Section J. Supporting references

S1. M. Yuasa, K. Oyaizu, A. Yamaguchi and M. Kuwakado, *J. Am. Chem. Soc*., **2004**, *126*, 11128-11129.

S2. A. Palmgren, A. Thorarensen and J.-E. Bäckvall, *J. Org. Chem*., **1998**, *63*, 3764-3768.

S3. V. S. P. R. Lingam, R. Vinodkumar, K. Mukkanti, A. Thomas and B. Gopalan, *Tetrahedron Lett*., **2008**, *49*, 4260-4264.

S4. J. A. Mason, K. Sumida, Z. R. Herm, R. Krishna, J. R. Long, *Energy Environ. Sci.* **2011**, *4*, 3030.

S5. H. Wu, K. Yao, Y. Zhu, B. Li, Z. Shi, R. Krishna, J. Li, *J. Phys. Chem. C* **2012**, *116*, 16609.

S6. A. L. Myers, J. M. Prausnitz, *A.I.Ch.E.J.* **1965**, *11*, 121.

S7. R. Krishna, J. M. van Baten, *Chem. Eng. J.* **2007**, *133*, 121.

S8. R. Krishna, J. M. van Baten, *J. Membr. Sci.* **2010**, *360*, 323.

S9. R. Krishna, J. M. van Baten, *Phys. Chem. Chem. Phys.* **2011**, *13*, 10593.

S10. R. Krishna, J. M. van Baten, *J. Membr. Sci.* **2011**, *383*, 289.

S11. R. Krishna, J. M. van Baten, *J. Membr. Sci.* **2011**, *377*, 249.

S12. R. Krishna, J. M. van Baten, *Chem. Eng. Sci.* **2012**, *69*, 684.

S13. R. Krishna, J. R. Long, *J. Phys. Chem. C* **2011**, *115*, 12941.

S14. R. Krishna, *Microporous Mesoporous Mater.* **2014**, *185*, 30.

S15. R. Krishna, R. Baur, *Sep. Purif. Technol.* **2003**, *33*, 213.